X-642-68-310
PREPRINT

NASA TM X- 63312

PARAMETRIC ANGLES OF TRAJECTORY-DETERMINED FIELD LINE INTERSECTS

E. G. STASSINOPOULOS

JULY 1968

GSFC
GODDARD SPACE FLIGHT CENTER
GREENBELT, MARYLAND

X-642-68-310
PREPRINT

PARAMETRIC ANGLES OF TRAJECTORY-DETERMINED FIELD LINE INTERSECTS

E. G. Stassinopoulos

July 1968

GODDARD SPACE FLIGHT CENTER
Greenbelt, Maryland

ABSTRACT

Geomagnetic field lines are traced from points on a ballistic trajectory to the points where they cross a given altitude shell. The intersects thus obtained are called "trajectory determined intersects." Three parametric angles identify and describe their positions: the look-angles ψ and ϵ, azimuth and elevation respectively, which relate and intersect to a fixed location on the earth; and the line-angle α, which for an observer stationed at this fixed location is a measure of the divergence of the line-of-sight from the field line. The locus of all trajectory-determined intersects is the "intersect trace" at the specified altitude level.

The intersect trace of a sample rocket trajectory is obtained for the 100 kilometer level. The variations of the parametric angles with time and altitude are calculated for 19 ground locations distributed symmetrically around the launch site. For the specific flight path considered, there exists an area on the earth where optimum parametric angle conditions prevail, i.e., minimum changes in ψ and ϵ, and smallest values of α.

Finally, the observer-intersect distance is calculated for all stations.

CONTENTS

PARAMETRIC ANGLES OF TRAJECTORY-DETERMINED FIELD LINE INTERSECTS

by
E. G. Stassinopoulos
Goddard Space Flight Center

INTRODUCTION

An interesting and promising development in magnetospheric research is the introduction of controlled geophysical experiments.

The first proposal for such an experiment was made by Hess (1965), who suggested that a stream of electrons generated by a space-borne accelerator, could produce artificial auroras. These auroras would be powerful tools in understanding magnetic field line geometry, conjugate point locations, large scale magnetic and electric fields, auroral spectroscopy, plasma instabilities, and VLF generation. To evaluate the feasibility of the project, Hess suggested in a preliminary outline of a testing plan (private communication, 1967), that the initial apparatus be flown on an Aerobee 350 from Wallops Island.

In this report we investigate topological aspects of the experiment and appraise the position and orientation problems associated with visual or instrumental tracking of artificial auroral spots. We have chosen for study a nominal Aerobee 350 trajectory with a launch azimuth of 150 degrees, launch elevation of 87 degrees, and effective payload of 611 pounds.

To observe artifically generated auroras, especially with instruments of relatively small view angles, it is desirable to have advance knowledge of the approximate location where the auroral spots are expected to appear. If the particle source happens to move along a ballistic trajectory, as in the proposed experiment, the observational difficulties are compounded because to nearby observers the auroral path may sometimes look erratic. In fact, it will fluctuate strongly in azimuth and/or elevation if a station is within a "critical" range around the launch site. Rapid displacements of the spots in the field of view of the instruments are then to be anticipated.

Sudden and swift variations of the look angles for close-by observers could seriously impair the success of a costly experiment. A search-and-aim operation in real time could prove futile without some detailed prediction, owing to the short duration of actual beam-on intervals. This obstacle can be overcome if the operator anticipates these changes and knows beforehand in what direction they will move. He could, in fact, practice the motions in a sort of dry run, long before

the real launch. For this purpose a program has been designed which can approximately simulate such an experiment. Sample calculations were made with a theoretical flight path. Lines of force passing through selected points on this path were traced in the direction of the field. Their intersects with a set of successive altitude levels or "shells", ten kilometers apart, called "trajectory-determined intersects", were determined.

Three parametric angles identify and describe the position of those intersects: the look-angles ψ and ϵ, azimuth and elevation respectively, which relate an intersect to a fixed location on the earth; and the line-angle α, which for an observer stationed at this fixed location is a measure of the divergence of the line-of-sight from the field line.

The "intersect trace" or locus of all such intersects for the 100-km shell was obtained. Parametric angles for 19 strategically placed stations were computed. The results were plotted versus time and the "critical" range was established. A region of optimum-parametric-angle-conditions emerged.

PARAMETERS OF PROBLEM

Trajectory, L-band, Time Limitations

The trajectory used for the computations is within the launch capability of the Wallops Island facilities; it pertains to an Aerobee 350 rocket with an effective payload of 611 pounds launched at 150° azimuth and 87° elevation. Owing to the low latitude of the launch site and the southeasterly direction of the impact zone, it crosses relatively few "L-shells". The L-band traversed by the flight path is shown in Figure 1; it has a mean value of about 2.56 earth radii.

Field lines were traced only for points on the trajectory above 150 km. This limited the study to the time interval bounded by $t' = 110$ and $t' = 460$ seconds, where the prime indicates "after liftoff". The evaluation of the parametric angles was further restricted to $200 < t' < 400$ seconds because during the initial phase of the flight, that is for $t' < 200$ seconds, unsettled conditions prevail.

Specifically, until its burn-out at about $t' = 55$ seconds, the rocket is affected by perturbations which may cause the actual trajectory to deviate substantially from that originally planned. An accurate prediction of the true path to be followed by the rocket cannot be made on the basis of initial conditions, such as launch azimuth or elevation, payload, and thrust. Maneuvers and activities, required to stabilize the vehicle, orient the apparatus to the field direction, and deploy the ion collecting screen usually would be scheduled during the 145 seconds following burn-out. Furthermore, any other task or function that may be necessary prior to the activation of the experiment would be performed then.

During the terminal phase of the flight, when $t' > 400$ seconds, the increasing speed of the descending vehicle hampers effective tracking of the spots with instruments of narrow view angles. Therefore, with regard to parametric angles, the best time for conducting experiments lies between 200 and 400 seconds after liftoff.

Stations

Figure 2 depicts the location of the nineteen stations selected for investigation; it also shows the launch site, the horizontal projection of trajectory points 10 seconds apart, and the corresponding intersects at 100 km altitude; furthermore, the position of the peak altitude point is indicated and the beginning of the "prime" time interval for experiments is marked.

At first, eleven reference stations were placed in a circle around the peak altitude intersect. This arrangement, yielding more information on the look-angle-to-position relationship than any other pattern, also saves valuable computer time. Later, eight more stations were added in a linear formation to investigate the parametric angles along a line parallel to the main segment of the intersect trace.

METHOD

Field Line Tracing and Altitude Intersects

A method developed by the author for geomagnetic field line tracing was presented in a previous paper (Roederer et al., 1966). A brief review of this method is given here in Appendix A. The procedure used in this report is essentially the same, with only minor modifications to adapt it to the present work.*

The magnetic field strength and field vector components are calculated with McIlwain's new MAGNET subroutine (part of the INVAR subroutine), employing the 99-term geomagnetic field model by Hendricks and Cain (1966) for the epoch 1960.0, updated to 1965.0.† The L-parameter is computed with Hassit and McIlwain's new (1967) INVAR subroutine.

The field line integration stepsize, a constant of the tracing process, was set to 2 kilometers; tests with larger elements of arc had produced disproportionate errors in the position of the intersects, up to ±1 degree in latitude and/or longitude, while still expending almost the same computer time.

Lines were traced in the direction of the field only.

The Look-Azimuth ψ

The azimuth of a point in space C relative to a position $\underline{a}$ on a sphere is the angle between the meridian plane through $\underline{a}$ and the plane $S(\underline{a}, \underline{b}, 0)$, measured clockwise from the northern direction

*The following changes were introduced into the line tracing procedure: The direction of the tracing was not reversed, since no conjugate intersects were needed; the quantities "arclength", "dip", and "declination" were of no concern and were not computed; no search for the existence and location of a minimum-B point was made; the L computing part was retained without the value test; the section that calculates the intersects was extended to permit their calculation at several consecutive altitude levels during each tracing operation.

†This model is best known as the GSFC 9/1965. It is available from the National Space Sciences Data Center at Goddard Space Flight Center, Greenbelt, Maryland 20771.

of the reference meridian (Figure 3a). The angle ψ in Figure 3b is the azimuth of C with respect to $\underline{a}$. From spherical trigonometry:

$$\psi = \arccos\left(\frac{\cos\theta_c - \cos\theta\cos\rho}{\sin\theta\sin\rho}\right) = \psi(\rho, \theta, \theta_c) . \tag{1}$$

For the geoid, when $\underline{a}$ and $\underline{b}$ are related to the known vectors $\bar{R}$ and $\bar{R}_c$ (Figure 1), θ and θ_c are constants and $\psi(\rho, \theta, \theta_c)$ is a function of ρ only. The cosine of ρ can be readily found from:

$$\cos\rho = \frac{\bar{R}\cdot\bar{R}_c}{RR_c} = \sin\theta\sin\theta_c\cos(\phi - \phi_c) + \cos\theta\cos\theta_c . \tag{2}$$

Thus, ρ is a function of the four position angles of $\underline{a}$ and $\underline{b}$. The azimuth of a field line intersect is easily determined from Equation 2.

The Look-Elevation ϵ

The elevation ϵ of a point in the sky with respect to an observer on the surface of the earth is the angle formed by the horizontal plane K and the line from the observer O to the point C as in Figure 4a. In a geocentric spherical coordinate system it is convenient to evaluate the elevation vectorially, in terms of the variables $\bar{R}$ and $\bar{R}_c$ and the angle ρ between them.

Let $\bar{Q}$ be some vector along the projection of $\bar{C}$ in the horizontal plane K, pointing away from the observer (Figure 4a). Obviously, in unit vector notation,

$$\sin\epsilon = \hat{C}\cdot\hat{R} , \tag{3}$$

$$\cos\epsilon = \hat{C}\cdot\hat{Q} . \tag{4}$$

We see from Figure 4b that

$$\hat{C} = \frac{1}{|\bar{C}|}\left(R_c\hat{R}_c - R\hat{R}\right), \tag{5}$$

and from Figure 4c and 4d that

$$\hat{Q} = \frac{\left(\bar{R}\times\bar{R}_c\right)\times\bar{R}}{|\bar{Q}|} \tag{6}$$

These relations give:

$$\epsilon = \sin^{-1}\left(\frac{1}{|\bar{C}|} R_c \cos\rho - R\right),$$

$$= \cos^{-1}\left(\frac{1}{|\bar{C}|} R_c \sin\rho\right). \tag{7}$$

The Line-Angle α

In the southern magnetic hemisphere, the angle formed by a descending field line $\bar{B}$ and the line of sight $\bar{C}$ of an observer will be called the "line angle" and will be represented by α (Figure 5a). Obviously

$$\cos\beta = \frac{\bar{C}\cdot\bar{B}}{CB} = -\cos\alpha. \tag{8}$$

Since

$$\bar{C} = \bar{R}_c - \bar{R} = \hat{i}\left(R_{c_x} - R_x\right) + \hat{j}\left(R_{c_y} - R_y\right) + \hat{k}\left(R_{c_z} - R_z\right), \tag{9}$$

the cartesian components are

$$\left.\begin{aligned} C_x &= R_{c_x} - R_x = R_c \sin\theta_c \cos\phi_c - R\sin\theta\cos\phi, \\ C_y &= R_{c_y} - R_y = R_c \sin\theta_c \sin\phi_c - R\sin\theta\sin\phi, \\ C_z &= R_{c_z} - R_z = R_c \cos\theta_c - R\cos\theta. \end{aligned}\right\} \tag{10}$$

Since a unit vector conversion in Equation 9 leads to

$$\left.\begin{aligned} C_r &= C_x \sin\theta_c \cos\phi_c + C_y \sin\theta_c \sin\phi_c + C_z \cos\theta_c, \\ C_\theta &= C_x \cos\theta_c \cos\phi_c + C_y \cos\theta_c \sin\phi_c - C_z \sin\theta_c, \\ C_\phi &= -C_x \sin\phi_c + C_y \cos\phi_c, \end{aligned}\right\} \tag{11}$$

the spherical components are

$$
\begin{aligned}
C_r &= \bar{C} \cdot \hat{r} = R_c - R \cos\phi \,, \\
C_\theta &= \bar{C} \cdot \hat{\theta} = -R \left[\sin\theta \cos\theta_c \cos(\phi_c - \phi) - \cos\theta \cos\theta_c \right] \,, \\
C_\phi &= \bar{C} \cdot \hat{\phi} = R \sin\theta \sin(\phi_c - \phi) \,.
\end{aligned}
\tag{12}
$$

Recalling that

$$
B_r \hat{r} + B_\theta \hat{\theta} + B_\phi \hat{\phi} = \bar{B} = \nabla V \tag{13}
$$

where the potential V is given by the well known function

$$
V = \sum \left(\frac{a}{r} \right)^{n+1} P_n^m(\theta) \left(g_n^m \cos\phi + h_n^m \sin\phi \right) \,, \tag{14}
$$

we obtain the components of $\bar{B}$:

$$
\left.
\begin{aligned}
B_r &= \frac{\partial V}{\partial r} \,, \\
B_\theta &= -\frac{1}{r} \frac{\partial V}{\partial \theta} \,, \\
B_\phi &= \frac{1}{r \sin\theta} \frac{\partial V}{\partial \phi} \,,
\end{aligned}
\right\} \tag{15}
$$

for increasing r, θ, and ϕ. The coordinate system used is illustrated in Figure 5b. The field components along the unit vectors $\hat{u}_v = -\hat{r}$, $\hat{u}_N = -\hat{\theta}$ and $\hat{u}_E = \hat{\phi}$ are

$$
\left.
\begin{aligned}
B_v &= -B_r \quad : \text{ vertically downward} \\
B_N &= -B_\theta \quad : \text{ horizontally north} \\
B_E &= B_\phi \quad : \text{ horizontally east}
\end{aligned}
\right\} \tag{16}
$$

The field calculations are performed with McIlwain's computer program MAGNET, using the 99-term Hendricks and Cain model for 1960.0 (GSFC-9/1965) updated to 1965.0. From the value of the field strength and the geometric considerations above, an accurate evaluation of Equation 8 is possible.

RESULTS

The results of our computations are given in Figures 6, 7, 8, 9, 10, and 11 in terms of parametric angles vs. time. Figures 12 and 13 give the spot-to-station distance with time. For a fixed altitude H, the look-elevation ϵ is strictly a function of the line-of-sight distance D:

$$\epsilon = \arccos \left(1 - H^2/D^2\right)^{1/2}$$

where $D = |\bar{C}|$.

Figure 14 is a plot of ϵ vs. D for H = 100 km. It may be used for quick determination of the approximate elevation, if the distance is known. Predictably, whenever ϵ is greater than 88°, the look-azimuth ψ becomes meaningless as a parameter for tracking. This condition exists when the intersect trace passes very close to, or over, a station. The effect on ψ of a near zenith passage of the spots is an abrupt jump in quadrants; it poses problems in adjusting instruments that cannot be moved through their local zenith. Stations No. 6 and 7 are affected most, whereas Stations No. 1, 2, 8, and 9, located well to the north or to the south along the extended projections of the main intersect segment, experience minimum variations in ψ. The consequence of these conditions is reflected, for the combined data of ϵ and ψ from all Stations, in Figures 15 and 16, which depict respectively "optimum" and "critical" look-angle areas on the ground.

In the context of this study, artificial auroras are spots generated by a rocket-borne accelerator that emits electron beam pulses of constant energy at intervals of three seconds. The electrons, interacting with the constituents of the upper atmosphere, are expected to produce the spots at an altitude which depends largely on their kinetic energy (Berger et al., 1968); the more energetic particles penetrating deeper into the atmosphere, the less energetic interacting at a greater height, (Figure 17). The sequential appearance of the spots in time should follow closely the intersect trace of that altitude level.

Corresponding to every rocket-generated intersect trace there exists an area on the ground where the auroras will be brightest for most of the duration of the flight above 150 kilometers, the luminance at a given location being proportional to a factor $k = 1/\sin \alpha$. Figure 18 shows the value of the luminosity factor over the range $0.5° < \alpha < 90°$.

Using the information available from Figures 10 and 11, the optimum α-area was determined on Figure 19 for $k > 2$ and $k > 3$. The apparent brightness of the spots may be of interest to some experimenters when selecting the site for a camera station.

From the evaluation of Figures 15, 16, and 19 the area of "Optimum Parametric Angle Conditions" emerges and the "Critical Range" develops, as shown in Figure 20. In the "Optimum Area", I corresponds to a luminosity factor of $k > 2$ and II to $k > 3$.

Finally, a station-centered polar look-angle plot is added as in Figure 21. It represents the intersect trace for each station plotted in ϵ vs. ψ.

ACKNOWLEDGMENTS

The author is grateful to Mr. Thomas Kelsall for reading the manuscript, and to Dr. H. L. Kyle for many helpful discussions and suggestions.

Goddard Space Flight Center
National Aeronautics and Space Administration
Greenbelt, Maryland, July 1968
188-48-01-99-51

REFERENCES

Berger, M. T., Kaichi Maeda and Steve Selzer, "Diffusion of Electrons in the Upper Atmosphere with a Constant Magnetic Field," to be published in *J. Atmos. Terr. Phys.*, 1968.

Hassit, A., and C. E. McIlwain, "Computer Programs for the Computation of B and L (May 1960)," NASA-NSSDC 67-27, May 1967.

Hendricks, S. J., and J. C. Cain, "Magnetic Field Data for Trapped Particle Evaluations," *J. Geophys. Res.*, 71:346, 1966.

Hess, W. H., "Electron Beam Field Mapping," Goddard Space Flight Center Document X-640-65-492, November 1965.

Roederer, J. G., W. H. Hess, and E. G. Stassinopoulos, "Conjugate Intersects to Selected Geophysical Stations," NASA Technical Note D-3091, July 1966.

Appendix

Field Line Tracing

The coordinate system used in the field line tracing process is illustrated in Figure 5b. The field components along the unit vectors $\hat{u}_v$, $\hat{u}_N$, and $\hat{u}_E$ are:

B_v : vertical down

B_N : horizontal north

B_E : horizontal east

The equations defining an infinitestimal portion of a line of force are:

$$\frac{\delta S}{B} = -\frac{\delta r}{B_v} = \frac{r\delta\lambda}{B_N} = \frac{r\cos\lambda\delta\phi}{B_E}$$

and δS is the element of arc, with components $-\delta r$, $r\delta\lambda$, and $r\cos\lambda\delta\phi$ along the unit vectors. The coordinates of a generic point of a field line originating at r_s, λ_s, and ϕ_s are then given by:

$$r_n = r_s + \sigma \sum_{i=1}^{n} \frac{B_{v_i}}{B_i} \delta S_i ,$$

$$\lambda_n = \lambda_s - \sigma \sum \frac{1}{r_i} \frac{B_{N_i}}{B_i} \delta S_i ,$$

$$\phi_n = \phi_s - \sigma \sum \frac{1}{r_i \cos\lambda_i} \frac{B_{E_i}}{B_i} \delta S_i ,$$

where the sign factor σ is ± 1 according to whether one proceeds tracing in the same direction as the field vector or the opposite. If the origin is in the magnetic southern hemisphere ($B_v < 0$), it is necessary to set $\sigma < 0$ in order to follow the descending line to the nearest intersect.

A four point "Adams integration formula" for numerical solutions of differential equations is used in the tracing procedure. Its repeated application at equidistant intervals approximates the field line. The accuracy of this fit depends on the integration step size.

FIGURES AND CAPTIONS

Figure

1 Range of magnetic shells crossed by Aerobee trajectory.

2 Map of stations with trajectory projection and 100-km intersect trace.

3 Geometry and relationships employed in evaluating the azimuth ψ in a spherical coordinate system.

4 Geometry of vectors and angles used in evaluating the elevation ϵ in a spherical coordinate system.

5 Geometry of vectors and angles used in calculating the line angle α.

6 Variation of look-elevation with time: Stations 1 to 9.

7 Variation of look-elevation with time: Stations 10 to 19.

8 Variation of look-azimuth with time: Stations 1 to 9.

9 Variation of look-azimuth with time: Stations 10 to 19.

10 Variation of line-angle with time: Stations 1 to 9.

11 Variation of line-angle with time: Stations 10 to 19.

12 Variation of distance with time: Stations 1 to 9.

13 Variation of distance with time: Stations 10 to 19.

14 Distance dependence of look-elevation for points on the 100-km. altitude shell.

15 Area of optimum look-angle conditions.

16 Critical ϵ and ψ area.

17 Approximate interaction altitude of electron beam.

18 Values of luminosity factor over the range: $.5^\circ \leq \alpha \leq 90^\circ$.

19 Optimum α area.

20 Area of optimum parametric angle conditions and critical range.

21 Station-centered polar look-angle plot.

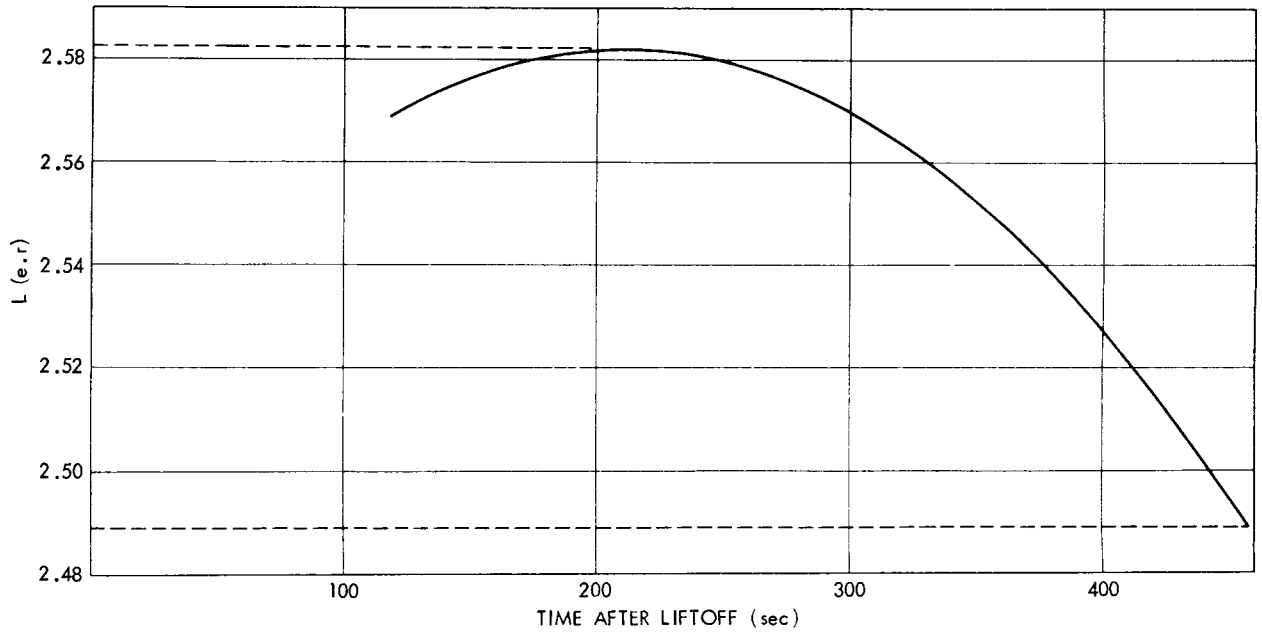

Figure 1–Range of magnetic shells crossed by Aerobee trajectory.

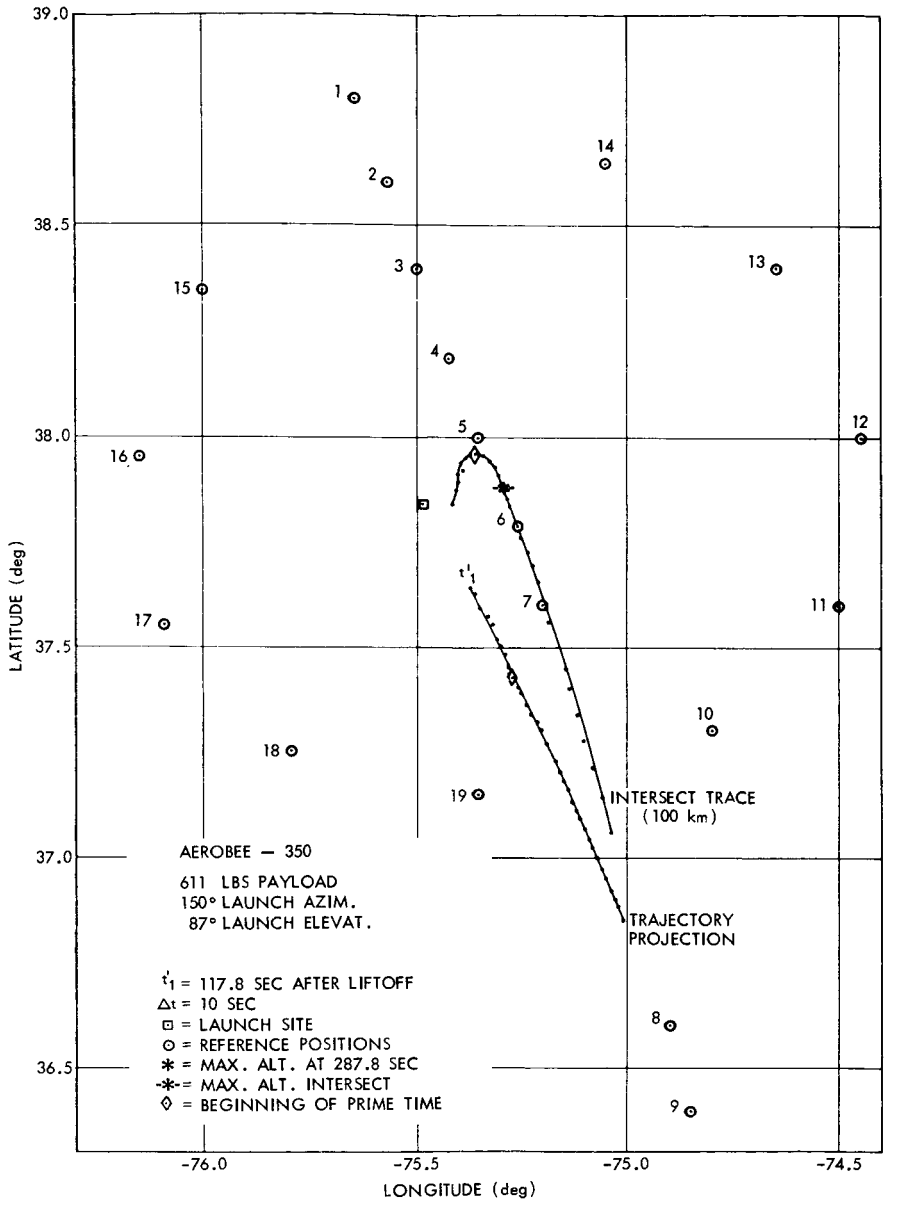

Figure 2–Map of stations with trajectory projection and 100-km intersect trace.

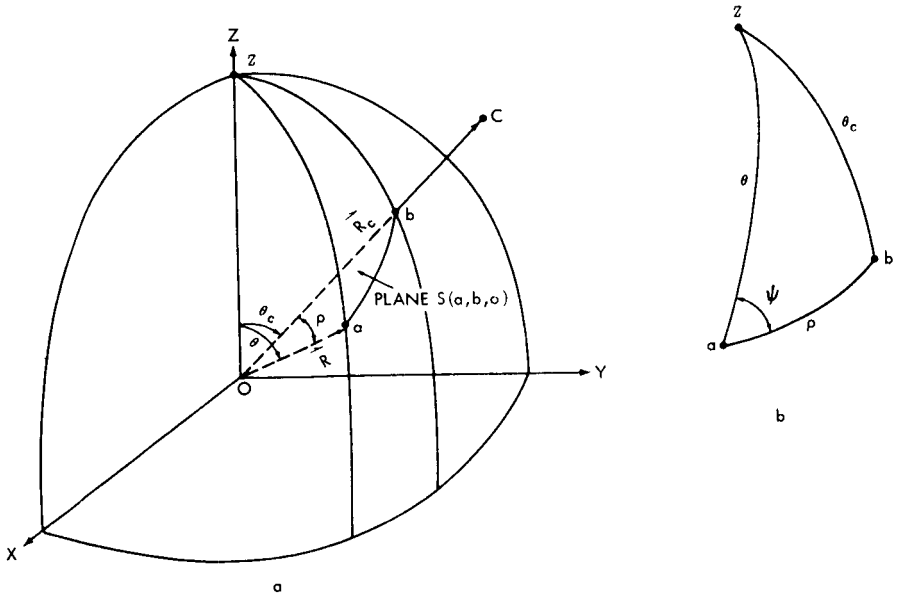

Figure 3–Geometry and relationships employed in evaluating the azimuth ψ in a spherical coordinate system.

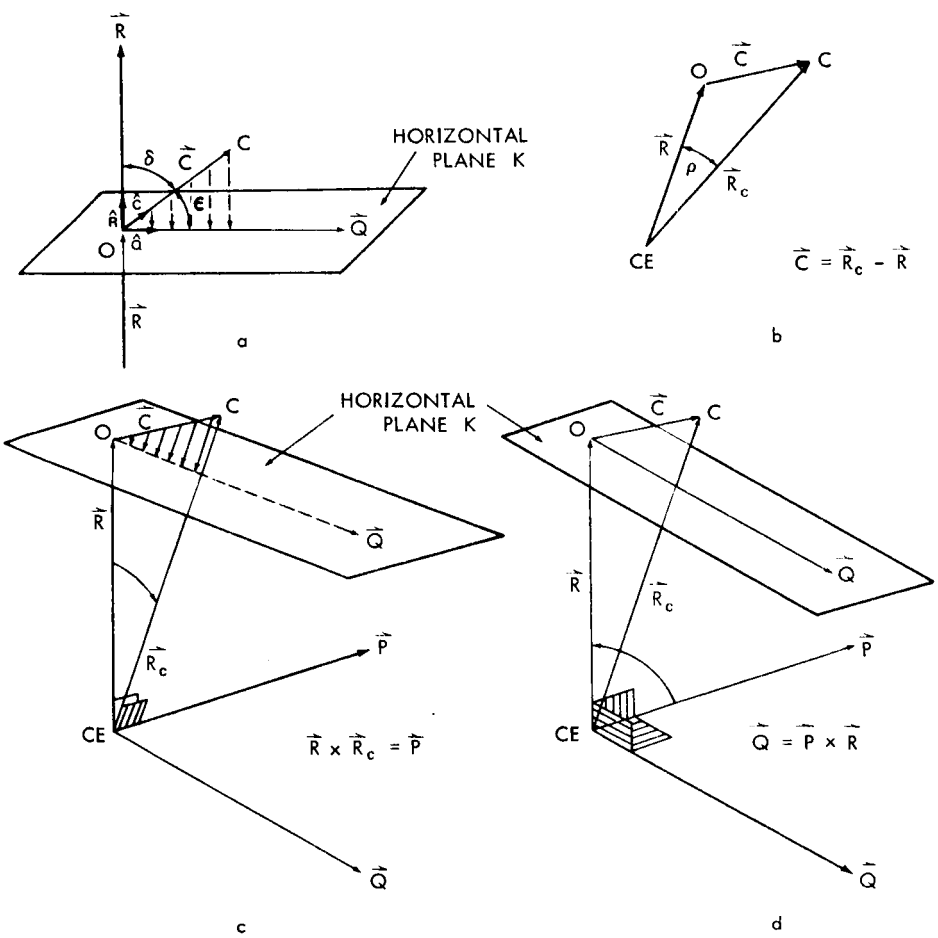

Figure 4–Geometry of vectors and angles used in evaluating the elevation ϵ in a spherical coordinate system.

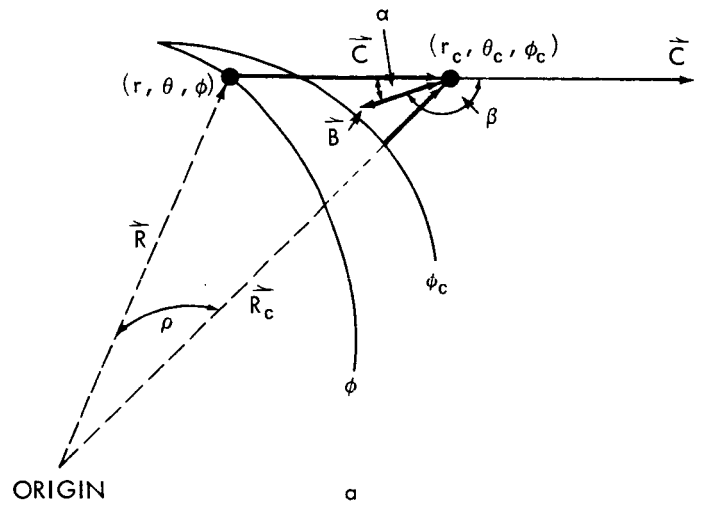

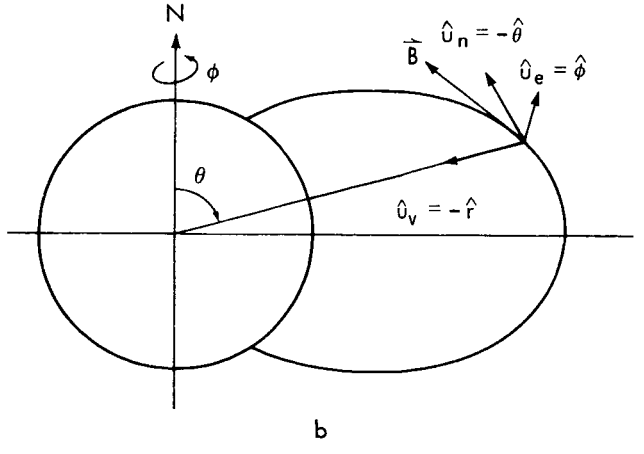

Figure 5–Geometry of vectors and angles used in calculating the line angle α.

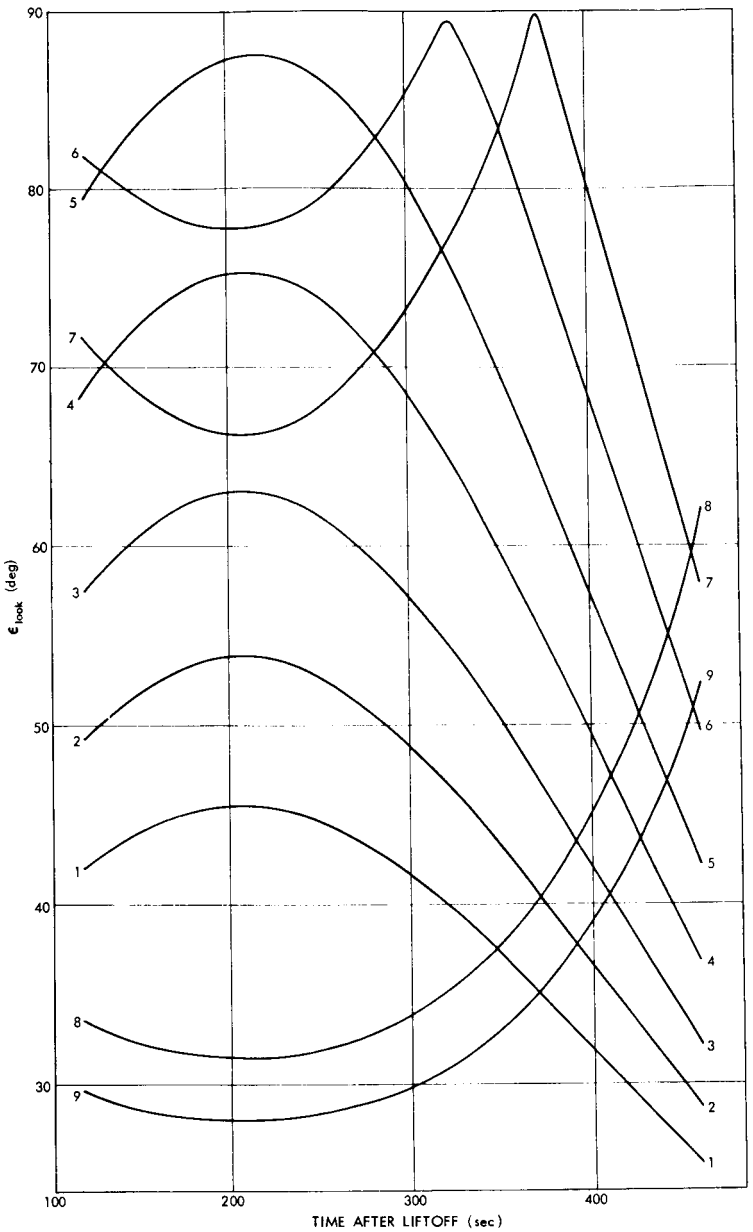

Figure 6–Variation of look-elevation with time: Stations 1 to 9.

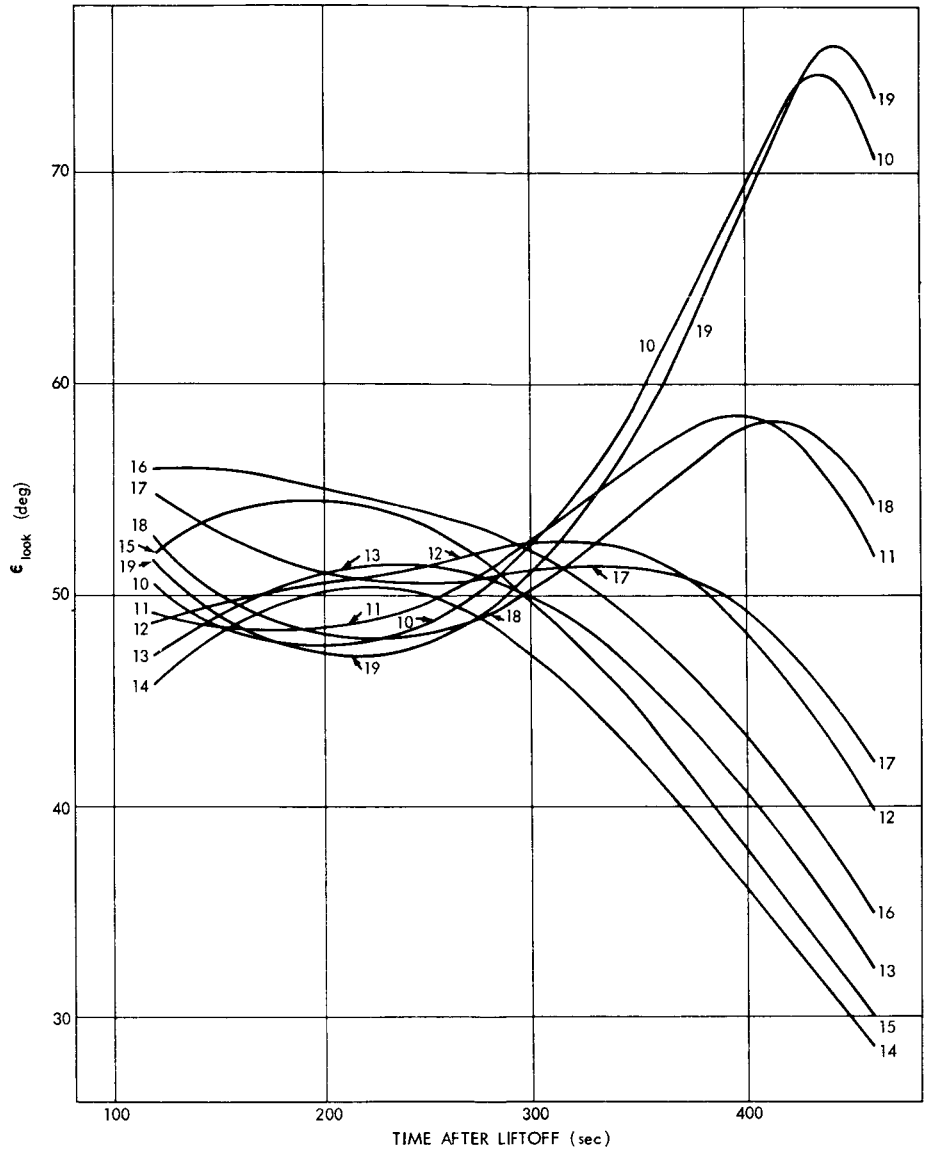

Figure 7–Variation of look-elevation with time: Stations 10 to 19.

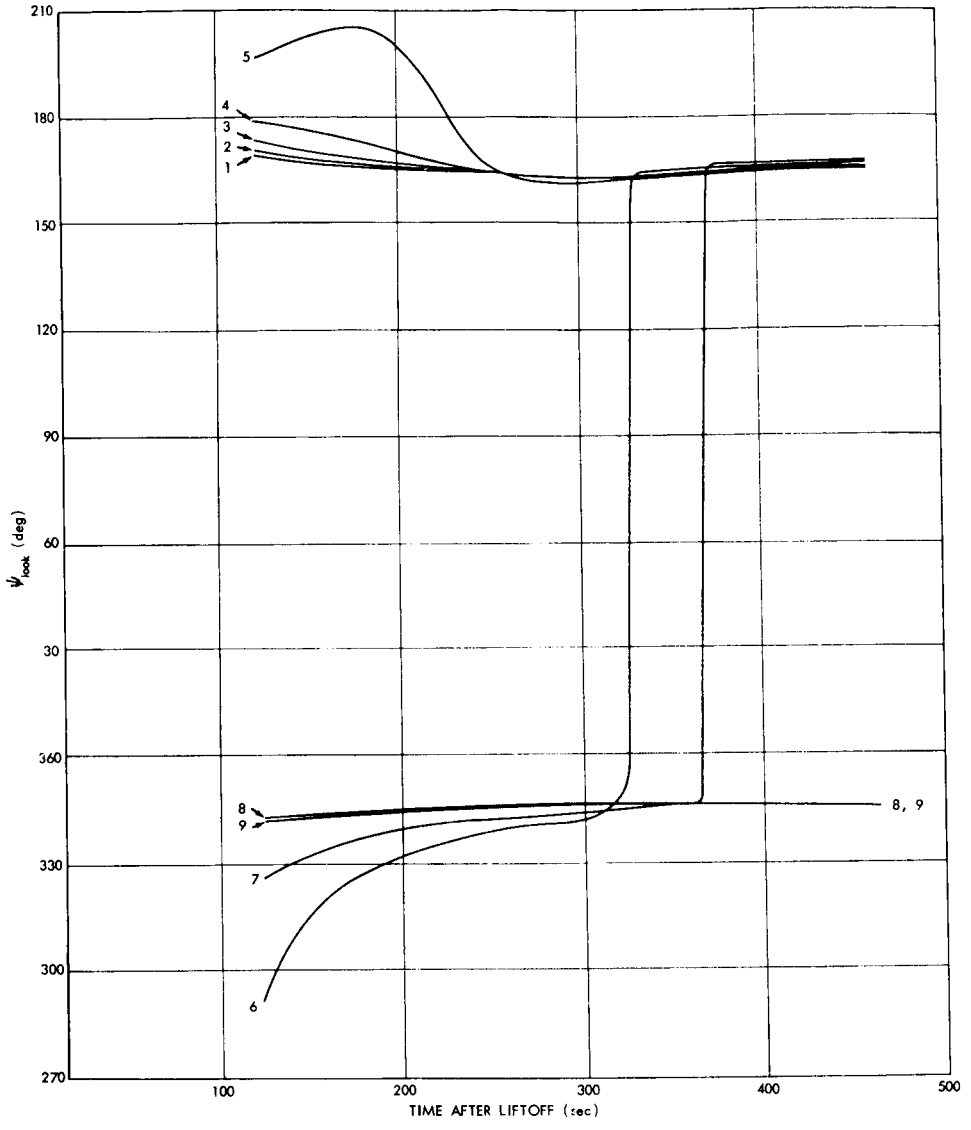

Figure 8–Variation of look-azimuth with time: Stations 1 to 9.

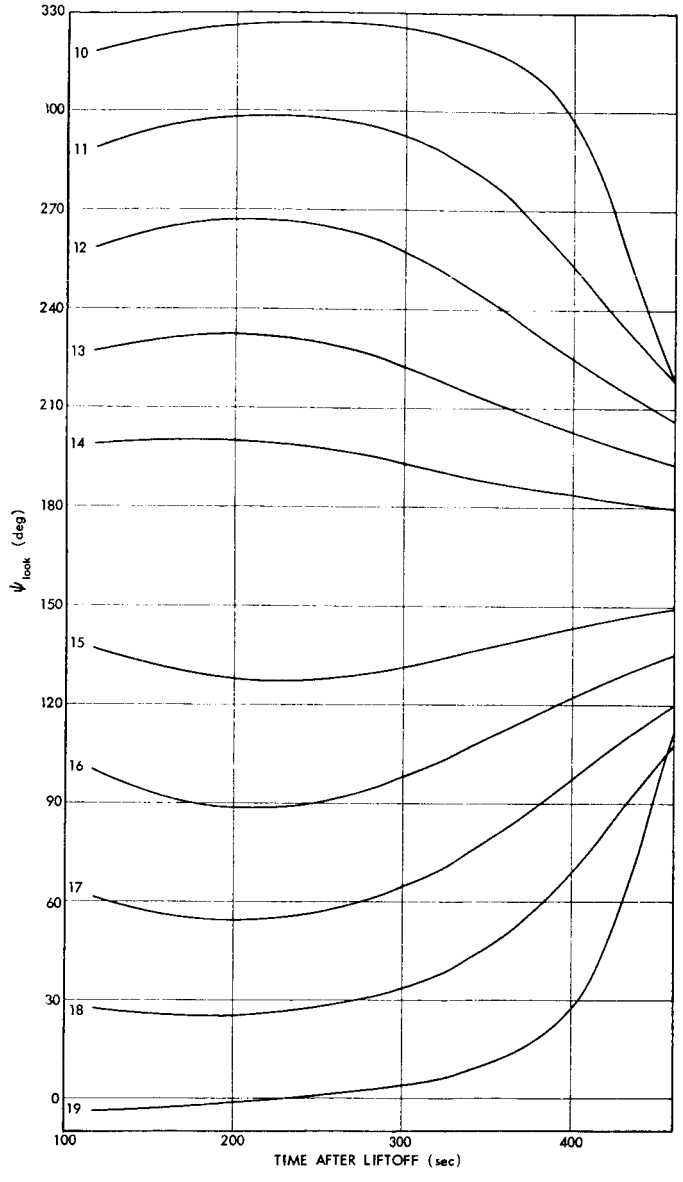

Figure 9–Variation of look-azimuth with time: Stations 10 to 19.

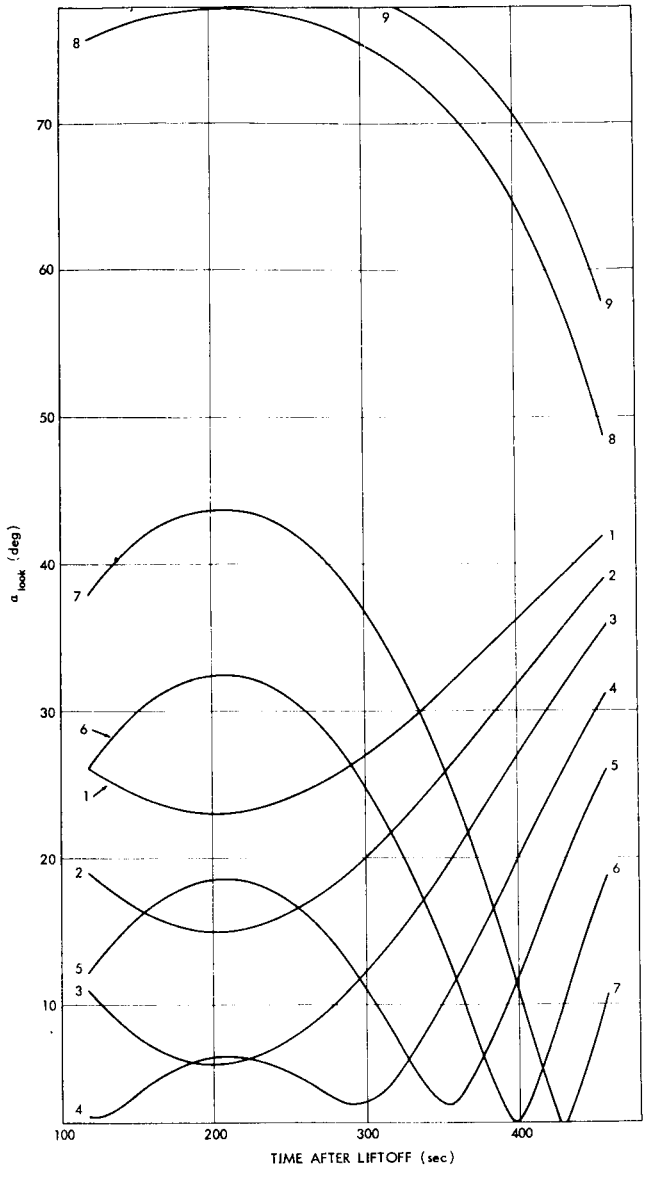

Figure 10–Variation of line-angle with time: Stations 1 to 9.

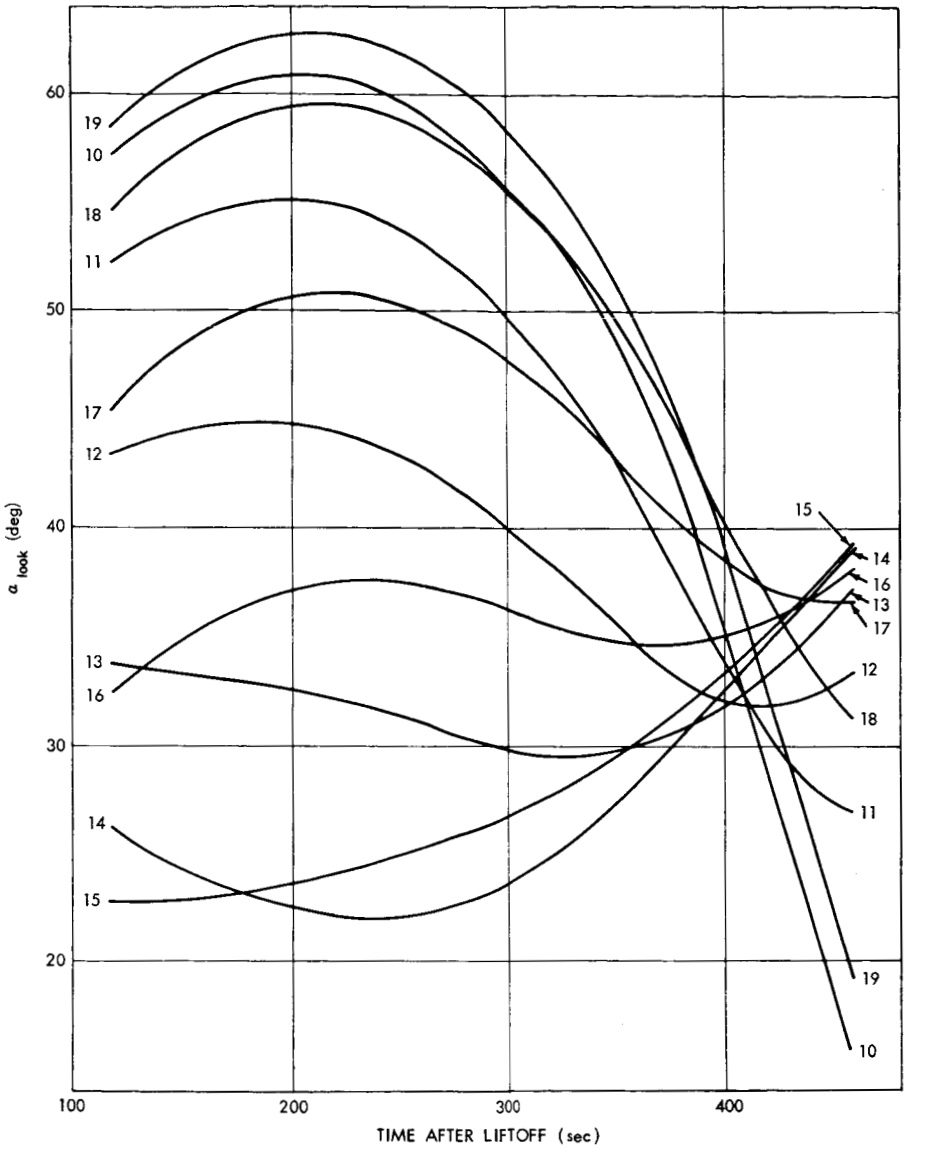

Figure 11–Variation of line-angle with time: Stations 10 to 19.

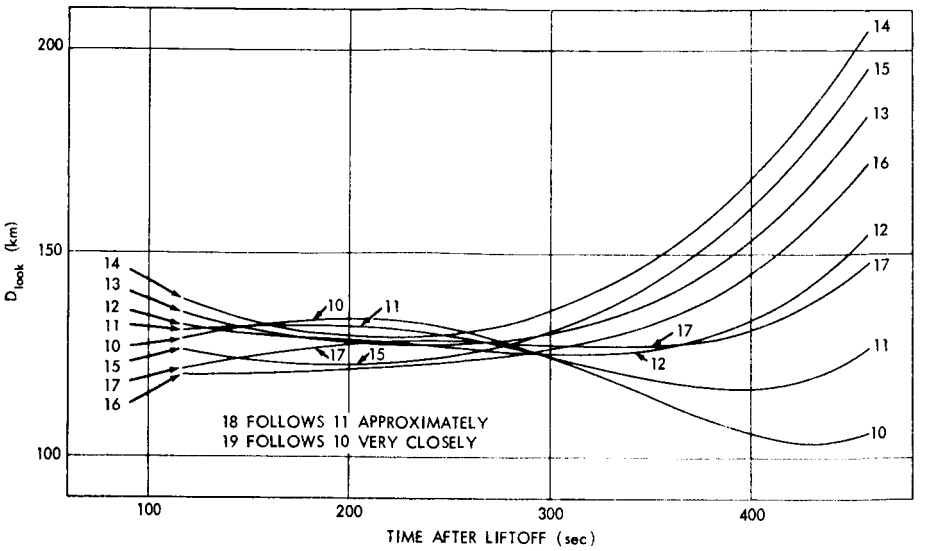

Figure 12–Variation of distance with time: Stations 10 to 19.

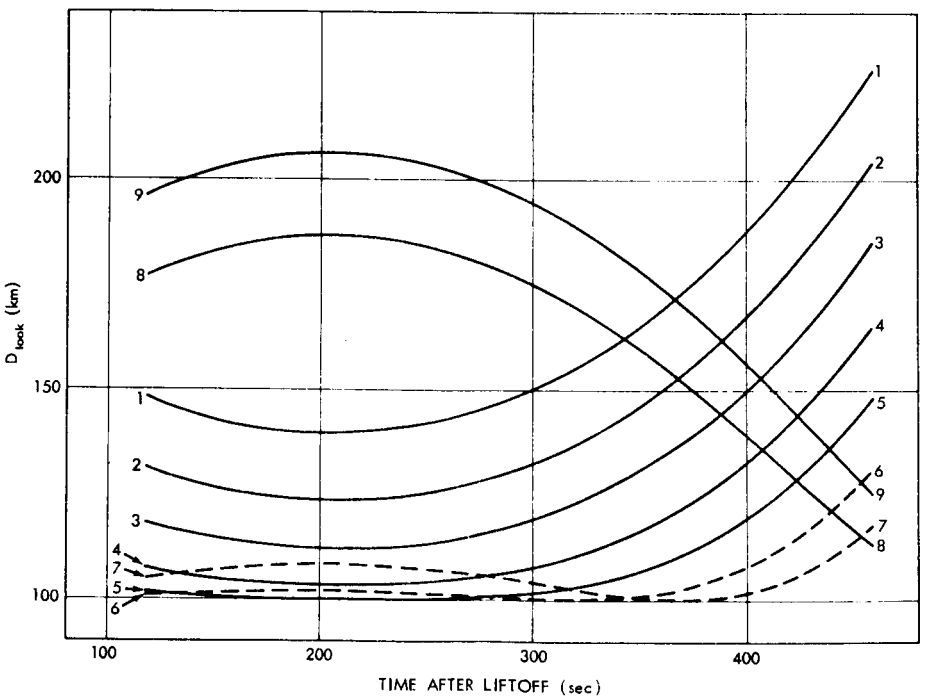

Figure 13–Variation of distance with time: Stations 1 to 9.

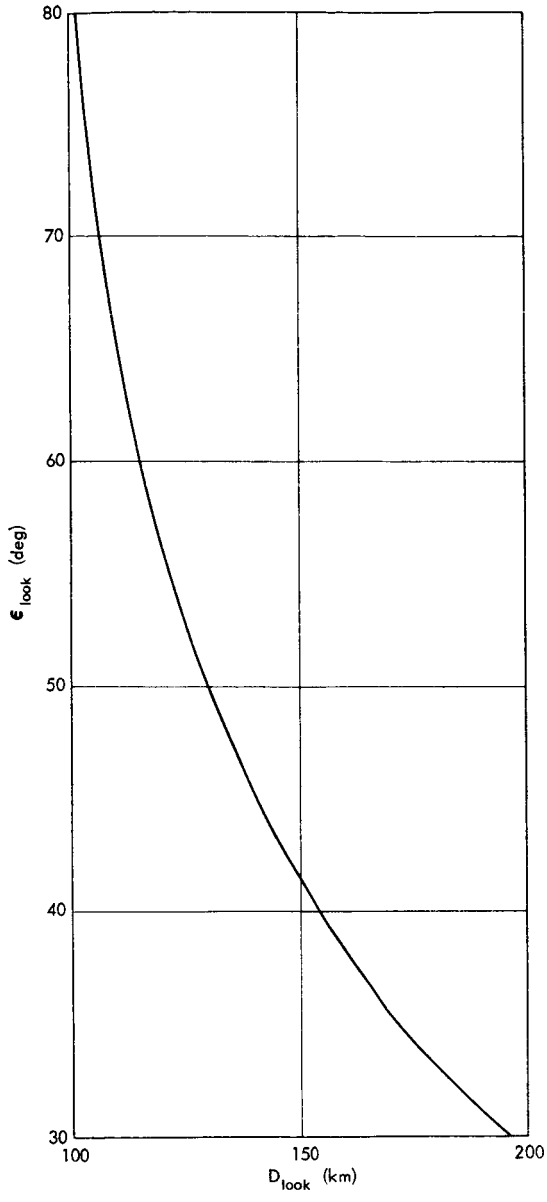

Figure 14–Distance dependence of look-elevation for points on the 100-km. altitude shell.

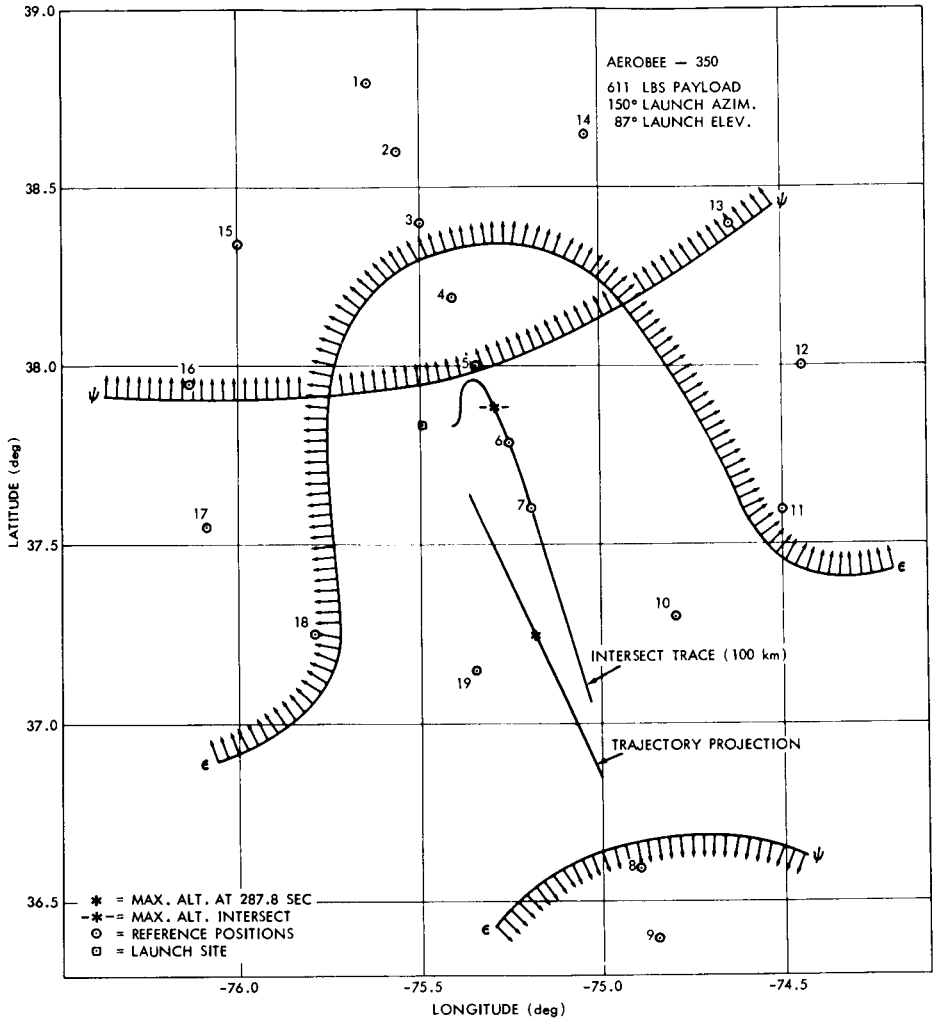

Figure 15–Area of optimum look-angle conditions.

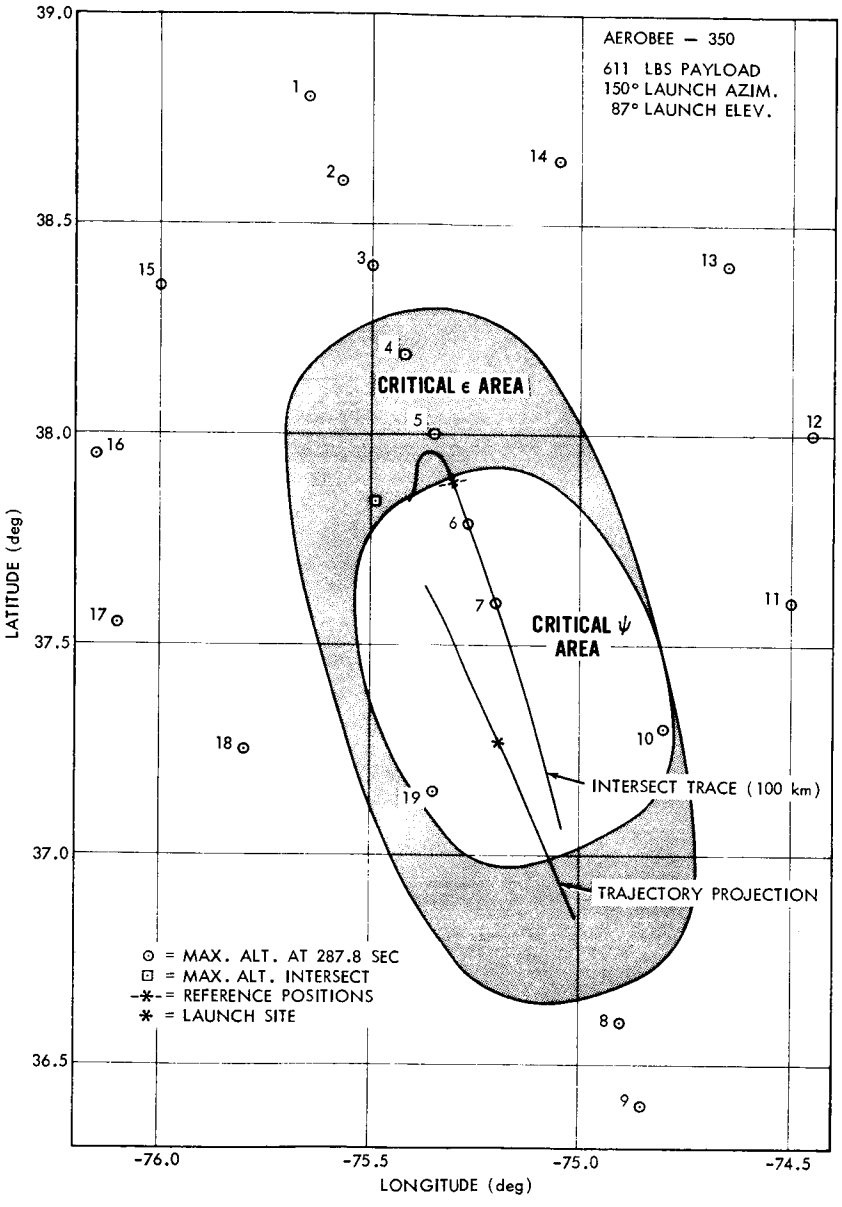

Figure 16–Critical ϵ and ψ area.

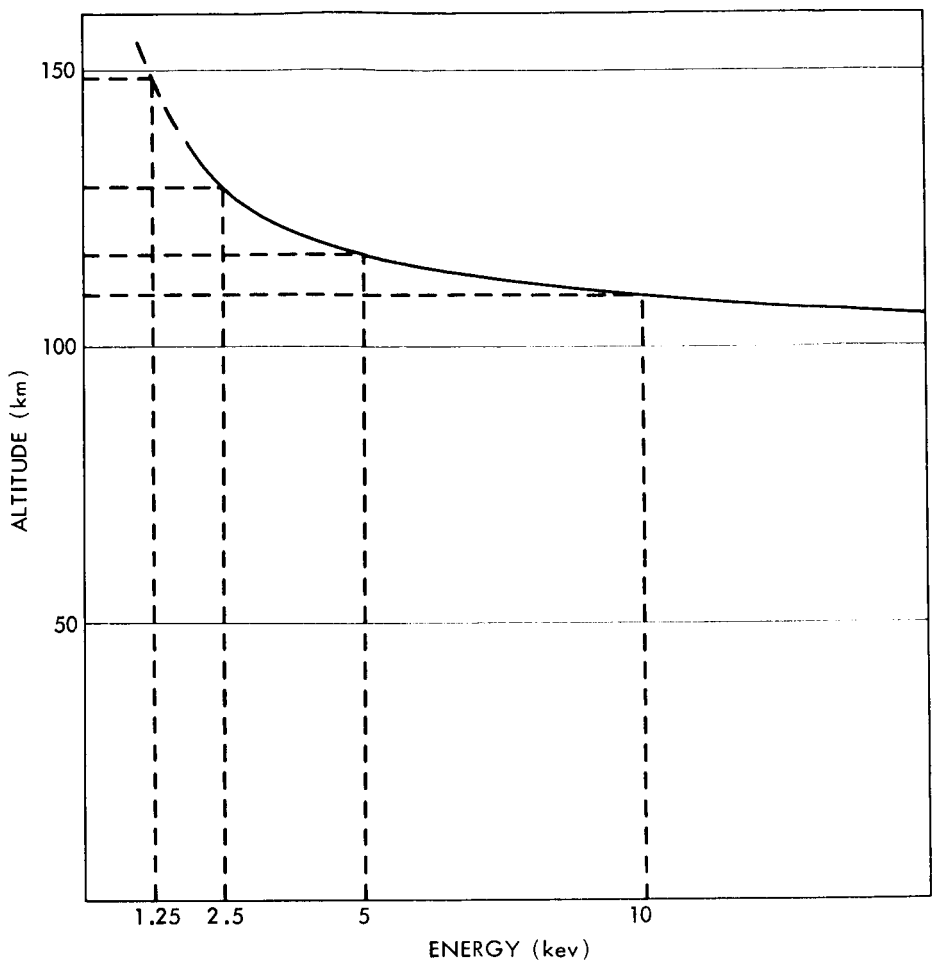

Figure 17—Approximate interaction altitude of electron beam.

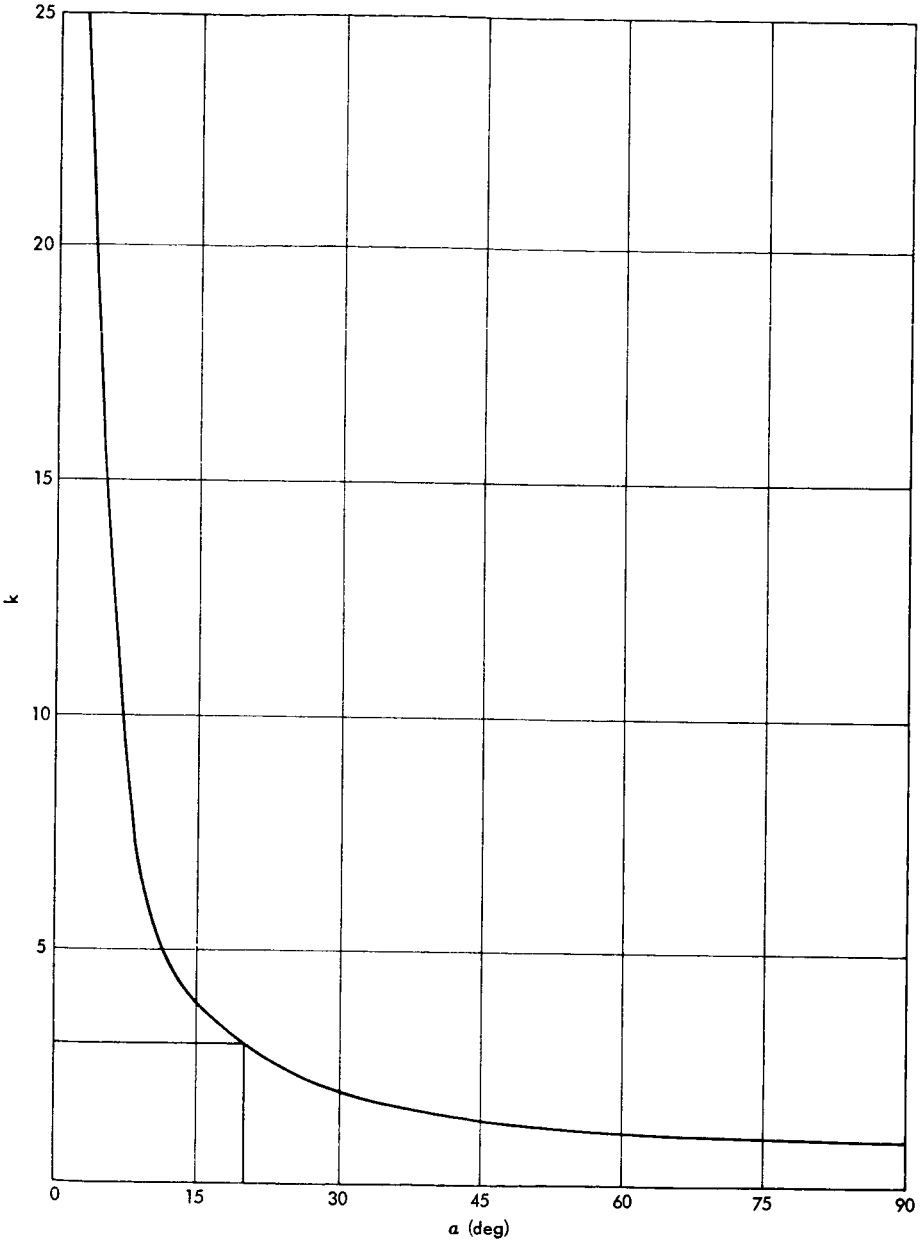

Figure 18–Values of luminosity factor over the range: $.5^{\circ} \leq \alpha \leq 90^{\circ}$.

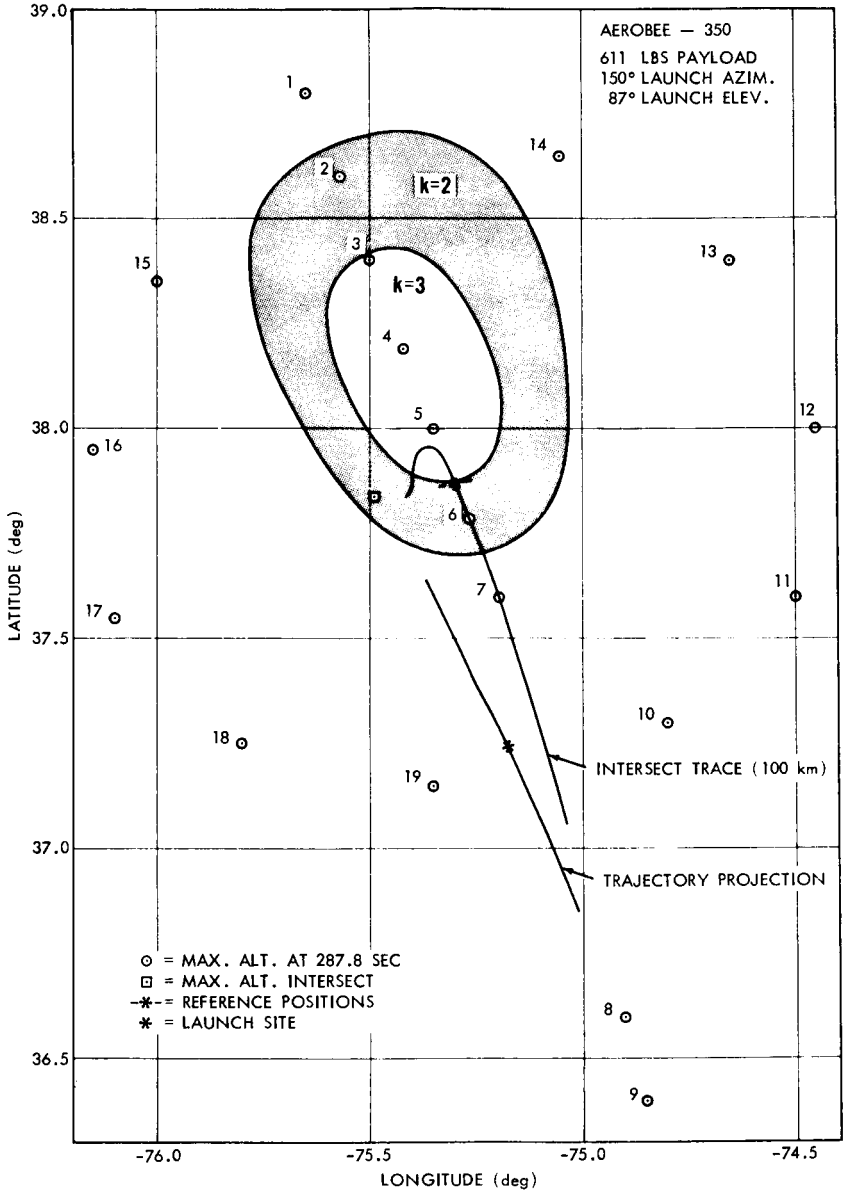

Figure 19—Optimum α area.

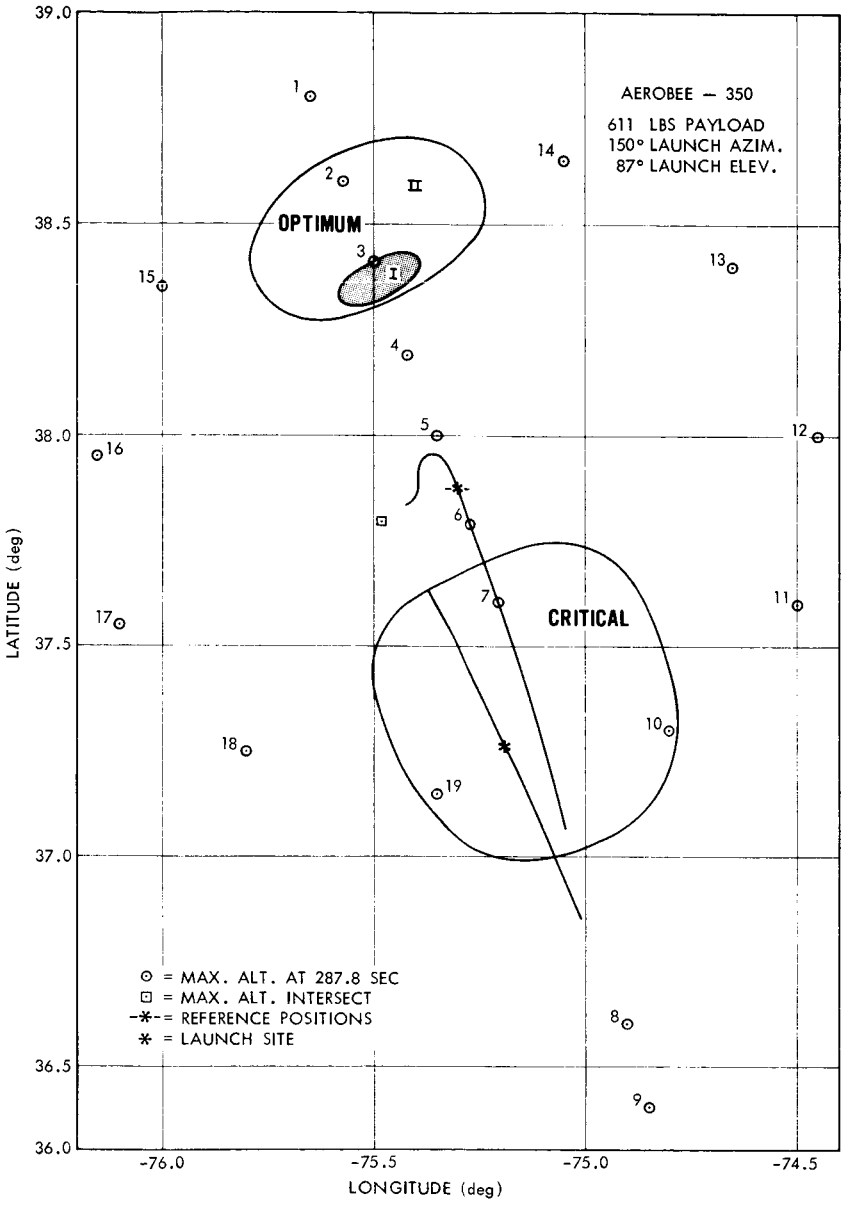

Figure 20–Area of optimum parametric angle conditions and critical range.

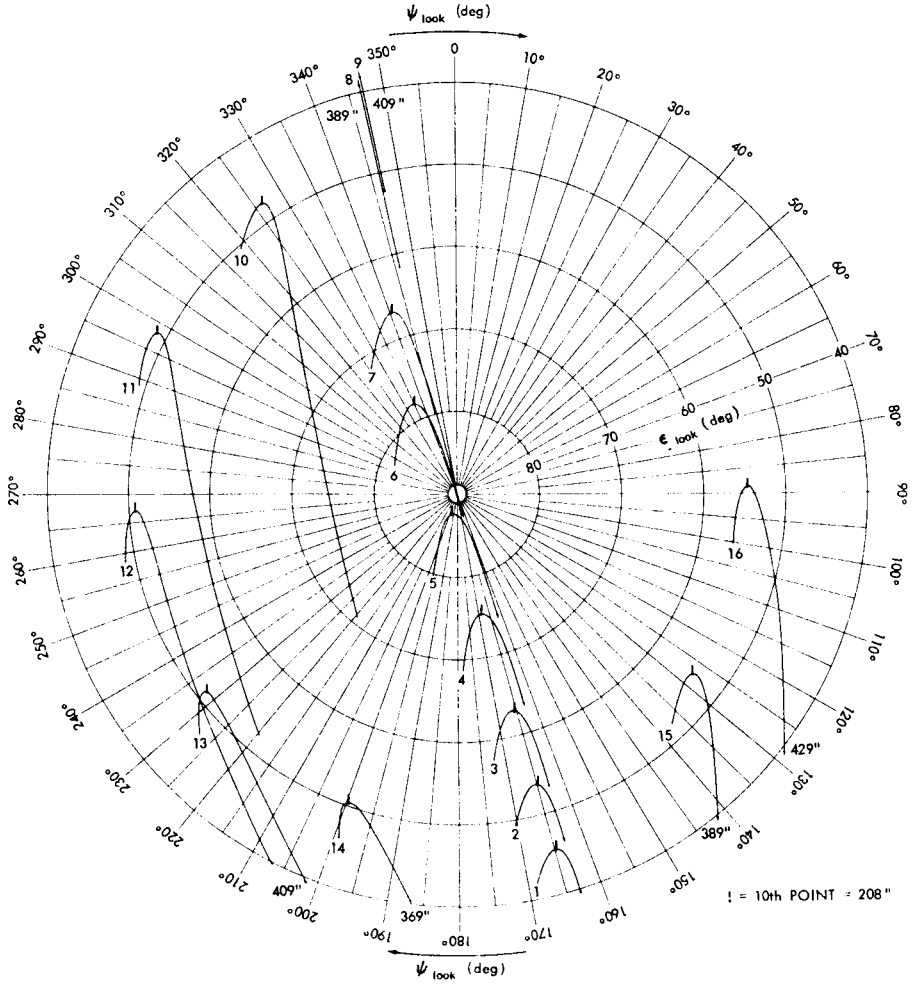

Figure 21–Station-centered polar look-angle plot.